Geomechanics and Engineering, *Vol. 23, No. 6 (2020) 587-600*
DOI: https://doi.org/10.12989/gae.2020.23.6.587

Shear failure and mechanical behavior of flawed specimens containing opening and joints

Yuanchao Zhang[1a], Yujing Jiang*[1], Xinshuai Shi[2], Qian Yin[2] and Miao Chen[3]

[1]*Graduate School of Engineering, Nagasaki University, 1-14 Bunkyo, Nagasaki 852-8521, Japan*
[2]*State Key Laboratory for Geomechanics and Deep Underground Engineering, China University of Mining and Technology, Xuzhou 221116, China*
[3]*College of Energy and Mining Engineering, Shandong University of Science and Technology, Qingdao 266590, China*

(Received April 29, 2020, Revised July 3, 2020, Accepted December 18, 2020)

Abstract. Shear-induced instability of jointed rock mass has greatly threatened the safety of underground openings. To better understand the failure mechanism of surrounding rock mass under shear, the flawed specimens containing a circular opening and two open joints are prepared and used to conduct direct shear tests. Both experimental and numerical results show that joint inclination (β) has a significant effect on the shear strength, dilation, cracking behavior and stress distribution around flaws. The maximum shear strength, occurring at β=30°, usually corresponds to a unifrom stress state around joint and an intense energy release. However, a larger joint inclination, such as β=90°~150°, will cause a more uneven stress distribution and a stronger stress concentration, thus a lower shear strength. The stress distribution around opening changes little with joint inclination, while the magnitude varys much. Both compression and tension around opening will be greatly enhanced by the 30°-joints. In addition, a higher normal stress tends to enhance the compression and suppress the tension around flaws, resulting in an earlier generation and a larger proportion of shear cracks.

Keywords: flaws; cracking; stress distribution; acoustic emission; PFC

1. Introduction

Joints exist widely in rock mass and are responsible for the discontinuity, inhomogeneity and anisotropy of the rock mass (Hoek and Brown 1997). The complex fracture network constitutes a potential failure path, and controls the mechanical behavior of rock mass (Lajtai 1969). When the rock mass is disturbed by external forces (e.g., earthquake force) or excavation, shear slip may occur along these pre-existing faults or joints, which seriously threatens the stability of the surrounding rock mass of opening, as shown in Fig. 1. Therefore, the failure and interaction mechanism between opening and joints under shear should be further investigated for a deeper understanding of the instability of surrounding rock mass.

In underground engineering, tensile failure usually occurs on the roof of opening, while the shear spalling usually appears at both sides (Gay 1976, Martin 1997, Fakhimi *et al.* 2002). Taking the circular opening as an example, Park (2017) revealed that tensile stress concentrations are mainly located at the top and bottom of opening, while the compressive stress concentrations occur at both sides of opening under a biaxial compressive state. However, when the openings are excavated near the joints, faults or weak planes, more complex and unconventional failures around the opening can be observed. For example, Jeon *et al.* (2004), Hao and Azzam (2005) have observed that faults or weak planes affect the stability of underground structure by the tendency of increasing the plastic zones, displacements and causing both asymmetrically distributed in the rock masses adjacent to the excavation. They finally attributed these to the activation or shear slip of fault or weak planes. Matsuki *et al.* (2009) further showed that the occurrence condition of fault significantly affected the stress evolution and movement characteristics of surrounding rock mass of underground excavations. To further explore the effect of joints or faults on the failure characteristics of openings, many simplified small-scale physical tests were conducted under the uniaxial and biaxial compression. For example, Sagong *et al.* (2011) observed the generation of interactive tensile cracks and removable blocks between the opening and joints. Fan *et al.* (2018) proved that the strength and deformation characteristics, stress distribution around the opening and joints are all highly dependent to the joint inclination. It is also found that failure intensity of the opening was related to the stress level, frictional coefficients of structural planes and time effect (Aksoy *et al.* 2020).

In this area of research, the method of numerical simulation is often used, combined with physical experiment, to explore the cracking mechanism and stress evolution of flaws in rock specimens. Particle flow code (Cundall and Strack 1979) is a powerful tool to simulate the

*Corresponding author, Professor
E-mail: jiang@nagasaki-u.ac.jp
[a]Ph.D. Student
E-mail: zhangyc4418@163.com, bb52219102@ms.nagasaki-u.ac.jp

ISSN: 2005-307X (Print), 2092-6219 (Online)

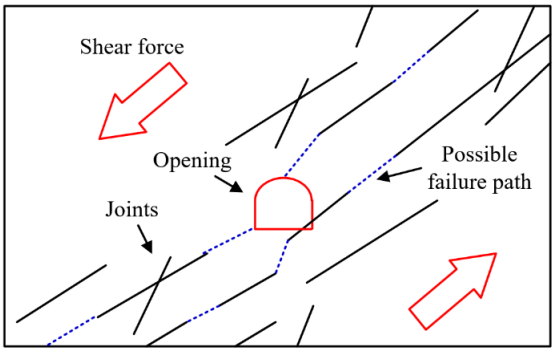

Fig. 1 Schematic diagram of shear-induced failure of jointed rock mass

Table 1 Physical and mechanical properties of the rock-like material in this research

	Density	Compressive strength	Elastic modulus	Poisson's ratio	Brazilian tensile strength	Cohesion	Friction angle
Unit	g/cm^3	MPa	GPa		MPa	MPa	°
Rock-like material	2.066	47.4	28.7	0.23	2.5	5.3	63.3
Sandstone	2.20-2.71	20-170	3-35	0.02-0.2	4-25	4-40	25-60

Table 2 The micro-parameters used in the PFC model

Micro-parameters	Value	Micro-parameters	Value
Minimum radius, R_{min} (mm)	0.4	Young's modulus of the parallel bond, E_c^* (GPa)	3.48
Ratio of radius	1.5	Ratio of normal to shear stiffness of parallel bond, K^*	1.25
Density, ρ (g/cm^3)	2066	Parallel-bond tensile strength, σ_t^* (MPa)	13.5
Young's modulus of the particle E_c (GPa)	3.48	Parallel-bond cohesion, c^* (MPa)	38.0
Ratio of normal to shear stiffness ofthe particle, K	1.25	Parallel-bond frictional angle, φ^* (°)	0.0

crack initiation, propagation and coalescence behavior and reveal the micro-level mechanical mechanism. For example, the cracking behavior of rock-like specimens containing single or multiple flaws has been investigated by using PFC (Bahaaddini *et al.* 2013, Manouchehrian *et al.* 2014). Recently, Yang *et al.* (2019) has revealed the coalescence mechanism between the opening and adjacent joints based on the mesoscopic displacement filed of particles in PFC.

Although many important results have been obtained by numerous experimental and numerical researches, they are almost all based on uniaxial or biaxial compression tests. So far, the failure and mechanical behavior of flawed rocks under shear has been rarely studied. In this research, the flawed specimens containing a circular opening and two joints were prepared using rock-like materials. Then, the direct shear tests under constant normal load (CNL) were conducted using a servo-controlled shear apparatus. Numerical shear tests were simultaneously performed based on particle flow code (PFC). Based on the experiments and numerical simulation, the shear strength and dilation, cracking damage and stress distribution of flawed specimens were discussed. The effect of joint inclination and normal stress were focused. Finally, some comparisons between shear and compression and some suggestions for direct shear tests of flawed specimens were made. This research is dedicated to a deeper understanding of shear-induced failure and mechanical behavior of surrounding rock mass when the opening is excavated in the jointed rock mass.

2. Experimental and numerical configuration

2.1 Specimens preparation

The flawed specimens were made of rock-like materials made by Jiang *et al.* (2004). This rock-like material was made of a mixture of plaster, water and retardant in a weight ratio of 1:0.2:0.005. Table 1 shows the physical and mechanical properties of this rock-like materials. It can be found that its mechanical parameters are similar to the sandstone (Zhuang *et al.* 2014), indicating that this rock-like material can well represent the mechanical properties of real rock material.

The geometric parameters of flawed specimens can be seen in Fig. 2(a). The joint inclination β changes from 0° to 150°, with an interval of 30°, as shown in Fig. 2(c). The other parameters remain unchanged. The numerical specimen is established based on parallel bond model and composed of 22340 rigid particles and more than 56000 contacts, as shown in Fig. 2(b). The joints and opening were generated by deleting particles. The parameters of particles

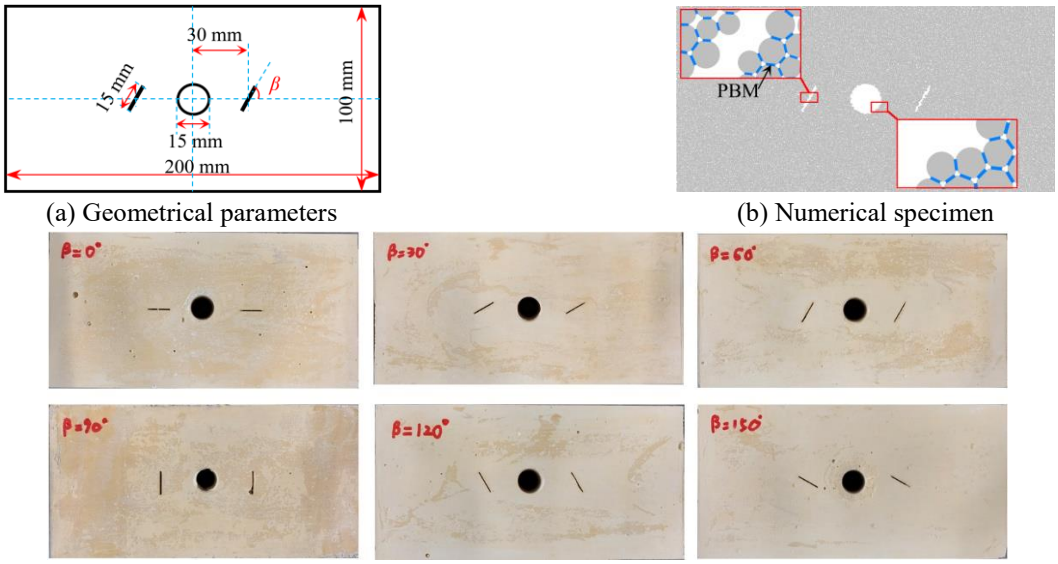

(a) Geometrical parameters (b) Numerical specimen

(c) Rock-like specimens

Fig. 2 Experimental and numerical configurations of flawed specimens

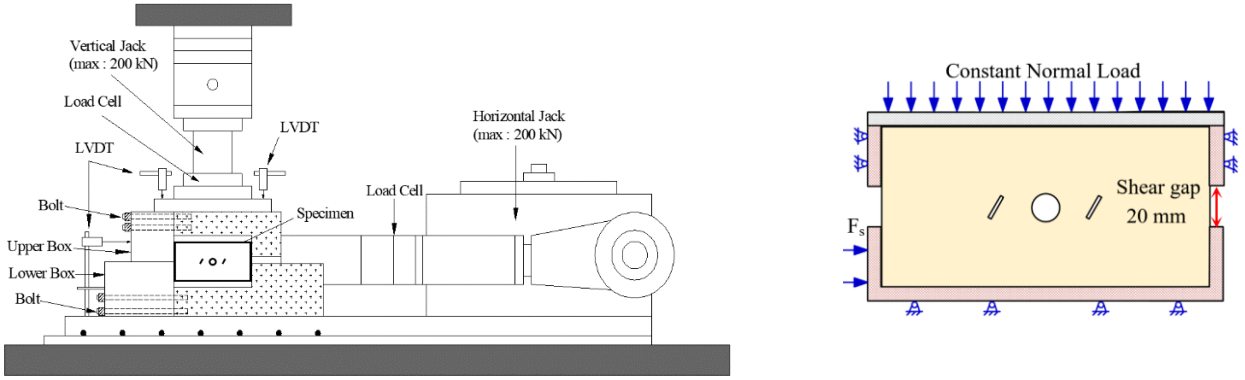

(a) Shear apparatus (b) Boundary conditions

Fig. 3 Shear apparatus and boundary conditions in direct shear tests

and bonds were continuously adjusted by the method of "trial and error", until the obtained macro-mechanical parameters were coincident with the rock-like materials. The calibrated micro-parameters of PFC were shown in Table 2. A detailed procedure can be referred to in Zhang *et al.* (2020).

2.2 Test methods

The servo-controlled direct shear apparatus designed by Jiang *et al.* (2004) was used to conduct the shear tests, as shown in Fig. 3(a). The maximum normal and shear load values of shear apparatus are 200 kN. The upper half of specimen is fixed in the horizontal direction, while the lower part is driven by the shear force (F_s), as shown in Fig. 3(b). The shear process was controlled by a displacement rate of 0.15 mm/min. The normal load, applied on the upper surface of shear box, remains unchanged during the shearing. The shear gap between the upper and lower shear boxes is 20 mm, slightly larger than the opening and joints size (15 mm). The boundary conditions of numerical shear tests are set exactly the same as the real direct shear tests.

The numerical shear displacement rate is set to 0.05 'm/s', which means that it requires approximately 260000 steps to reach a shear displacement of 1 mm, ensuring a quasi-static loading process. During the shear, the acoustic emission (AE) can be monitored by a PAC-AE system. The resonant frequency of the sensor was set to 50 and the operating frequency range from 100 kHz to 1 MHz. The amplification of the preamplifier and the threshold of the system were both set to 40 dB (Zhang *et al.* 2020).

3. Results and analysis

3.1 Shear strength

Fig. 4 shows the tested and numerical shear stress-shear displacement curves of specimens with different joint inclination under the normal stress of 1.0 MPa and 3.0 MPa. We can see that the numerical curves showed similar shear modulus (i.e., the slope of linear-elastic stage of curve) and peak strength as the tested results. Also, a large stress drop after peak, indicating a brittle failure, was highly consistent

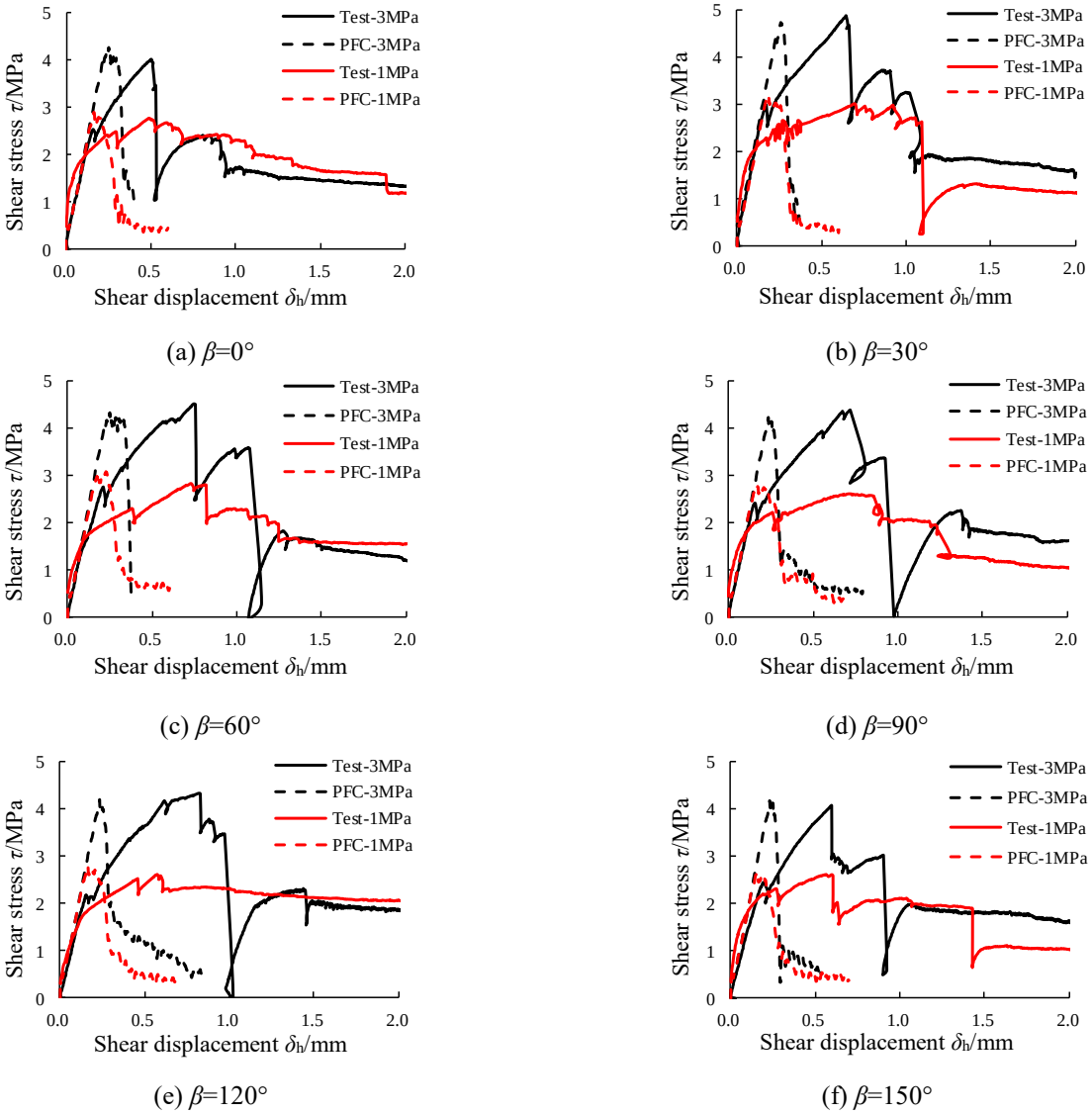

Fig. 4 The experimental and numerical shear stress-shear displacement curves of flawed specimens with different joint inclinations

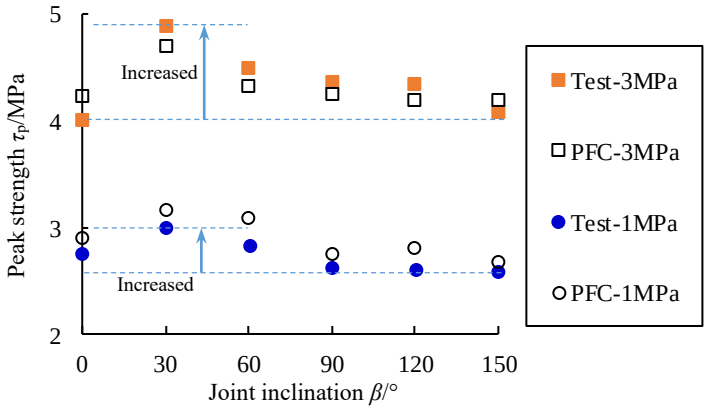

Fig. 5 The changes of peak shear strength with joint inclination

with the experiment results. However, the shear displacement, at which the peak stress occurs, shows a large gap between the test and PFC. This is because the tested curves show a more obvious non-linear deformation before the peak stress, which is hard for PFC to match.

Fig. 5 shows the changes of peak strength with joint

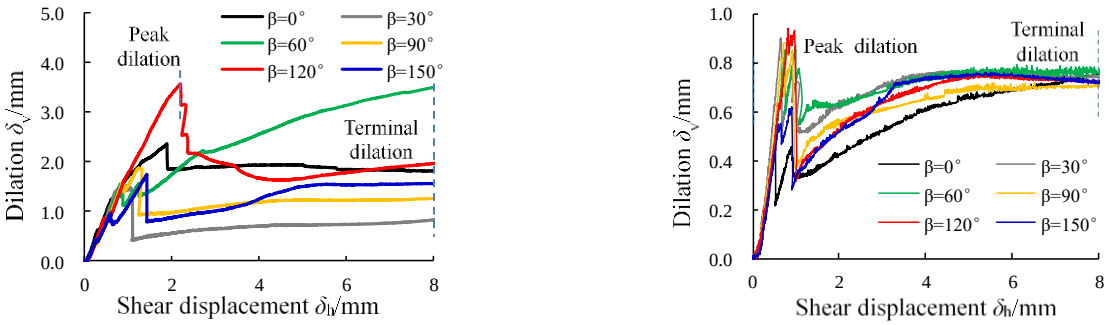

(a) σ_n=1.0 MPa (b) σ_n=3.0 MPa

Fig. 6 Experimental dilation curves of flawed specimens with different joint inclinations

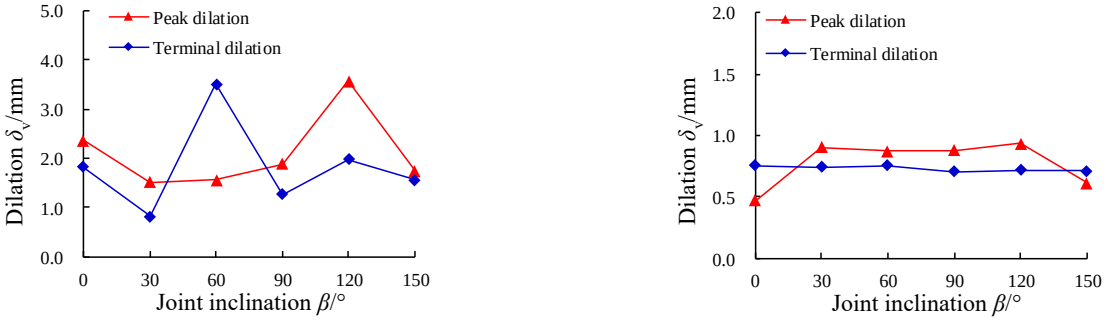

(a) σ_n=1.0 MPa (b) σ_n=3.0 MPa

Fig. 7 The changes of peak dilation and terminal dilation with joint inclination

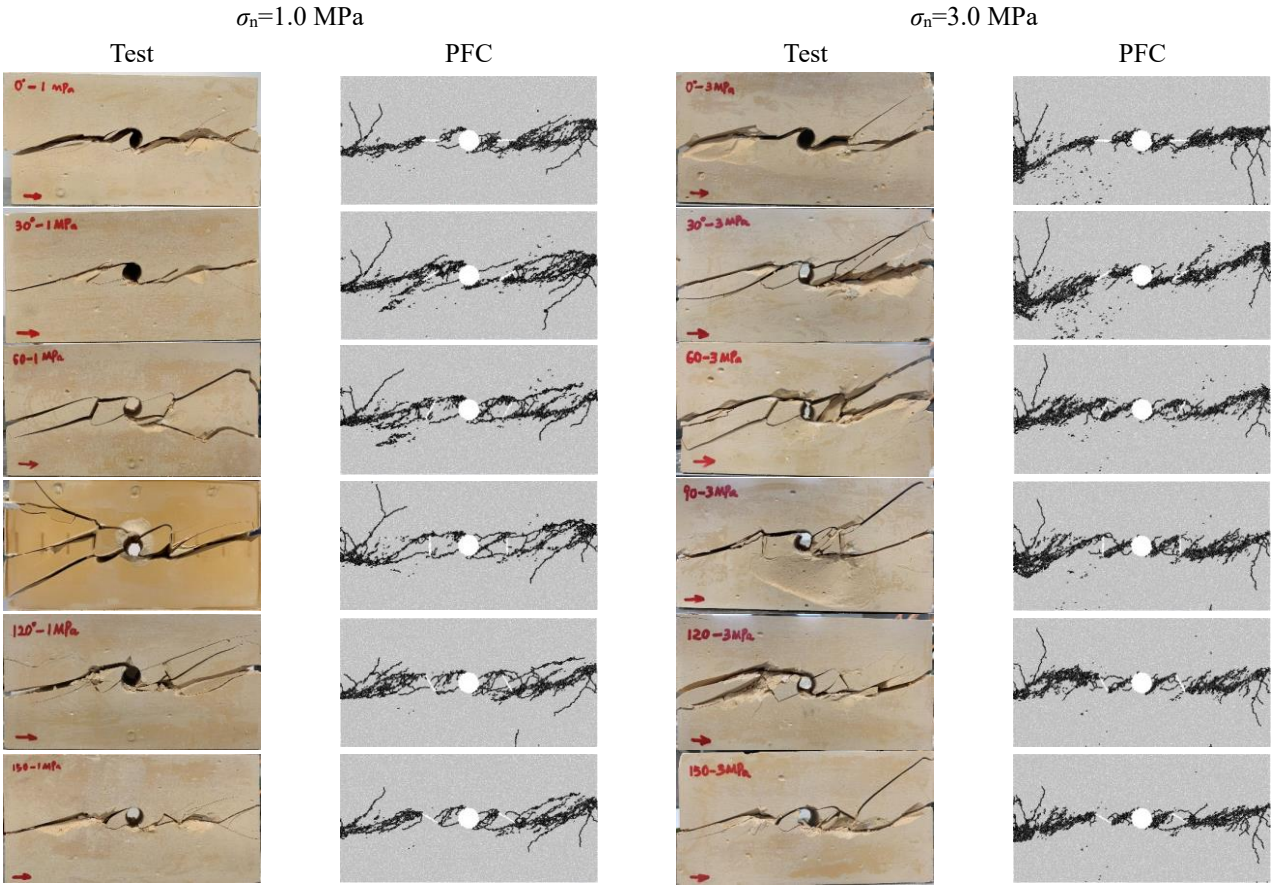

Fig. 8 Ultimate failures of flawed specimens under direct shear

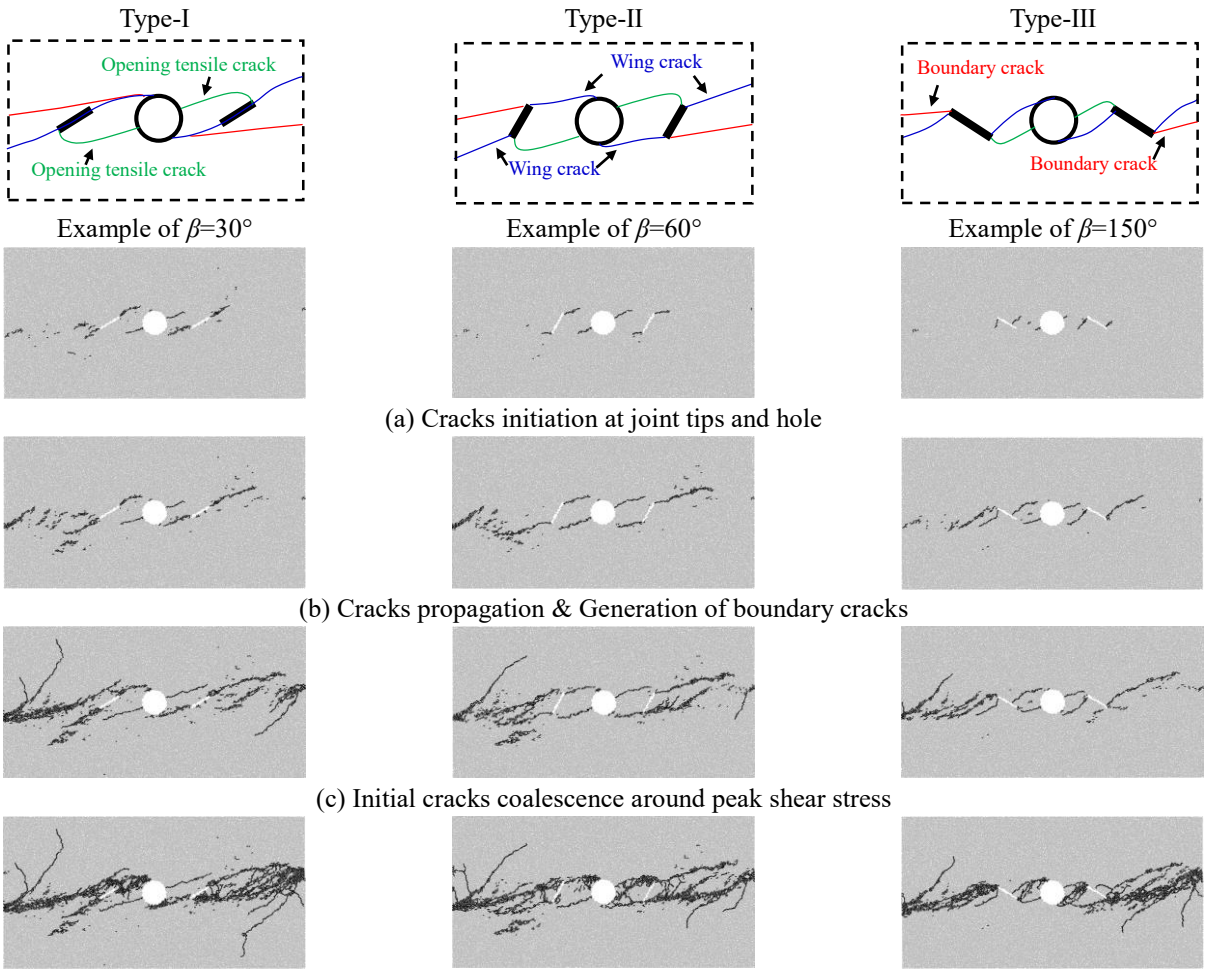

(a) Cracks initiation at joint tips and hole

(b) Cracks propagation & Generation of boundary cracks

(c) Initial cracks coalescence around peak shear stress

(d) Ultimate coalescence failure at post-peak stage

Fig. 9 Three basic failure patterns and cracking process of flawed specimens under direct shear

inclinations. The numerical results agree well with the test results. Both show that the shear strength firstly increases as β increases from 0° to 30°, then gradually decreases when β increases from 30° to 150°. Under various normal stress, the maximum shear strength occurs at β=30°. However, the minimum shear strength occurs at β=150° under the normal stress of 1.0 MPa, and β=0° under the normal stress of 3.0 MPa. In addition, a maximum increase of 22.1% can be observed under the normal stress of 3.0 MPa, which is larger than that of 1.0 MPa (15.5%), indicating that the effect of joint inclination on shear strength is more significant under a higher normal stress.

3.2 Dilation

Fig. 6 shows the normal displacement (or dilation)-shear displacement curves, recorded during the shear process. We can see that the dilation curves usually experienced three stages: (1) near-linear dilation before peak; (2) large contraction (i.e., dilation drop) near peak; (3) stabilization in post-peak stage. To evaluate the influence of joint inclination and normal stress on dilation, peak dilation δ_v^p and terminal dilation δ_v^t were used. Fig. 7 shows the changes of peak and terminal dilation with joint inclination under the normal stress of 1.0 MPa and 3.0 MPa.

From Fig. 7(a), we can see that, under the normal stress of 1.0 MPa, both δ_v^p and δ_v^t change obviously with joint inclination. The maximum δ_v^p occurs at β=120°, while the maximum δ_v^t occurs at β=60°, both near 3.5 mm. However, both minimum δ_v^p (about 1.5 mm) and minimum δ_v^t (about 0.8 mm) occur at β=30°. Fig. 7(b) shows that, under a higher normal stress of 3.0 MPa, δ_v^p and δ_v^t were greatly reduced, less than 1.0 mm, and changed not much with joint inclination. Only a lower peak dilation can be observed at β=0° and 150°. The above indicates that joint inclination has an obvious effect on the dilation behavior of flawed specimens, whereas the effect will be greatly weakened by the increasing normal stress.

3.3 Shear failure

Fig. 8 shows the failed specimens with different joint inclinations under the normal stress of 1.0 MPa and 3.0 MPa. The numerical failure patterns are highly consistent with those of real specimens, further indicating the reliability of numerical simulation. From Fig. 8 we can see that the shear failures of flawed specimens was complicated, and the failure patterns were closely related to the joint inclination. Overall, the shear failure of flawed specimen is mainly composed by two parts: (1) crack

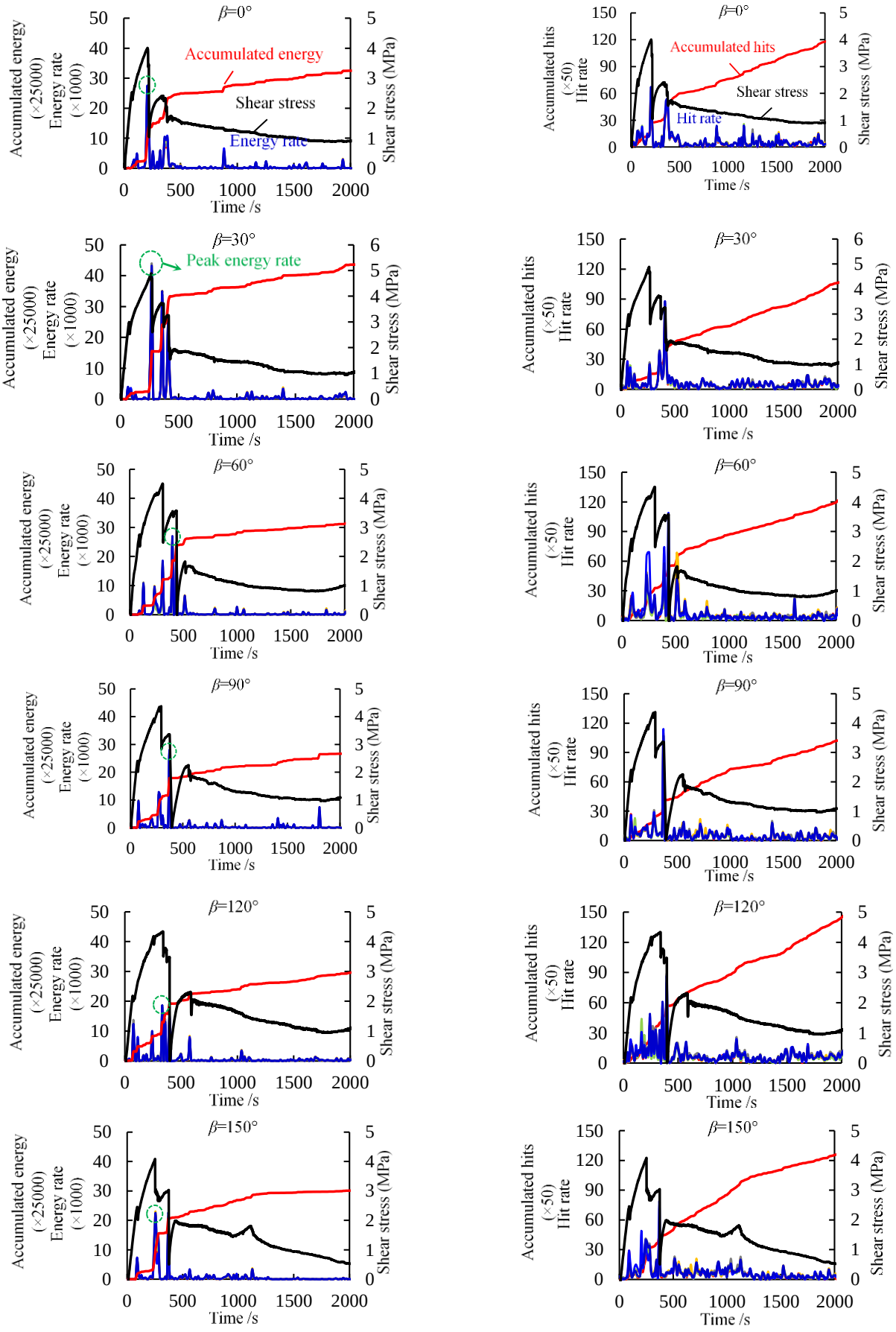

Fig. 10 The evolution of AE energy and hits of flawed specimens during the shear

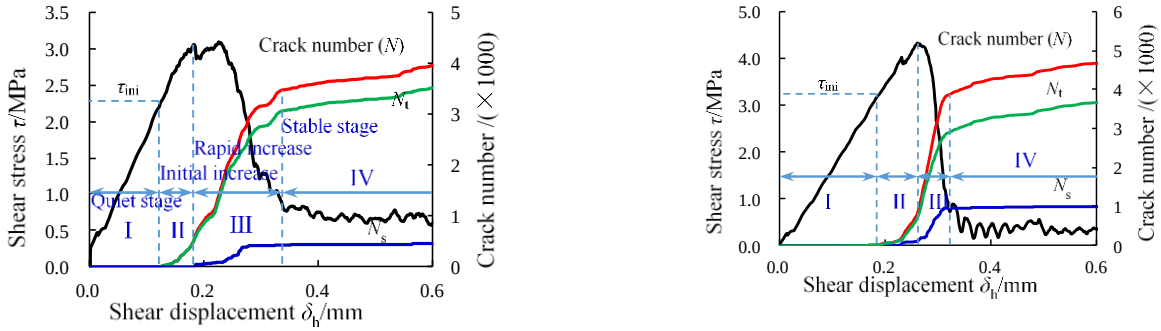

(a) σ_n=1.0 MPa (b) σ_n=3.0 MPa

Fig. 11 Evolution of the number of micro-cracks during the shearing (an example of β=60°)

coalescences between opening and joints and (2) crack coalescences between specimen boundaries and internal flaws. Usually, the coalescences between flaws were caused by the wing cracks that originate from the joint tips and tensile cracks that originate from opening. Large loose blocks can always be observed on both sides of opening and vary in size and shape with joint inclination. The failures between specimen boundaries and internal flaws were mainly caused by the boundary cracks that originated from the boundaries and wing cracks of joints.

Three basic failure patterns of flawed specimens under shear can be summarized in Fig. 9. Type-I can only be observed at β=30°, and Type-II mainly occurs at β=60° and 90°, while Type-III mainly occurs at β=0° and 150°. Especially, β=120° shows a transition type between Type-II and Type-III.

Fig. 9 also shows that, the progressive cracking process of three basic failure patterns were similar and mainly included four stages: (1) cracks initiation at joint tips and opening; (2) cracks propagation and generation of boundary cracks; (3) initial cracks coalescences around peak shear stress; (4) ultimate coalescence failure at post-peak stage. However, several differences can also be observed. For example, (1) the wing crack usually propagated obliquely or near perpendicular to the joint face in Type-II and Type-III, whereas it was coplanar with the joint face at β=30° (i.e., Type-I). (2) The micro-cracks usually firstly initiated from the joint tips, followed by the tensile cracks of opening in time. Whereas, the cracking sequence was reversed for β=30°. (3) The cracks tend to initiate at the middle part of joint when β=120°, which is quite different from the common situation that at the joint tips. The above differences may be attributed to the different stress state around the joints and openings caused by different joint inclinations, which were discussed later.

In addition, under the normal stress of 3.0 MPa, the failures of specimens are more intense. Those loose blocks near opening tend to be more broken and lots of surface spallings can be observed along the boundary cracks, as shown in Fig. 8. However, the increasing normal stress does not essentially change the shear failure petterns of flawed specimens.

3.4 AE characteristics

In recent years, acoustic emission (AE) has been increasingly used in damage assessment of in-situ rock mass (Kim *et al.* 2019). To evaluate the AE characteristics of flawed specimens during the shear, the evolution of AE energy and AE hits were recorded by the AE system. Fig. 10 shows the energy rate, hit rate, accumulated energy and accumulated hits of flawed specimens with different joint inclinations under the normal stress of 3.0 MPa. From Fig. 10, we can see that the entire shearing process can be divided into two stages, i.e., (1) coalescence failure stage, characterized by frequent stress drops and active AE events and (2) shear-slip stage, characterized by stable stress platform and quiet AEs. In the coalescence failure stage, each stress drop is usually accompanied by a sudden increase of energy rate and hit rate, which also causes a steep rise of accumulated energy and hits curves. In the shear-slip stage, low-level hit rate caused by the friction of fractures can be observed. Accordingly, the accumulated hits curve keeps growing. However, almost no large energy release occurs at this stage and the accumulated energy curve increases not much.

In addition, the magnitude of peak energy rate changes much with the joint inclination, indicating the difference of shear failure intensity caused by joint inclination. Fig. 10 shows that the maximum peak energy rate occurs at β=30°, about 4.3×10^4. The moderate magnitude occurs at β=60° and 90°, about 2.7×10^4. And the lowest peak energy rate occurs at β=120° or 150°, around 2.0×10^4. Combined with Fig. 5, we can find that the magnitude of peak energy rate is closely related to the shear strength. A higher shear strength, such as at β=30°, can result in a larger peak energy rate, indicating a more intense shear failure. Whereas, the shear failure with a lower shear strength tends to be more gentle.

4. Micro-cracks and stress distribution

4.1 Micro-cracks number

To further reveal the meso-damage characteristics of flawed specimens during the shearing process, the evolution of the number of micro-cracks was recorded in the simulation. Usually, the number of micro-cracks increased with the shear displacement and experienced four stages, i.e., quiet stage, initial increase, rapid increase and stable stage, as shown in Fig. 11. The number of tensile cracks is always much larger than that of shear cracks, indicating that

(a) At peak stress (b) At the stable stage

Fig. 12 The number ratio of shear cracks to tensile cracks at peak stress and stable stage

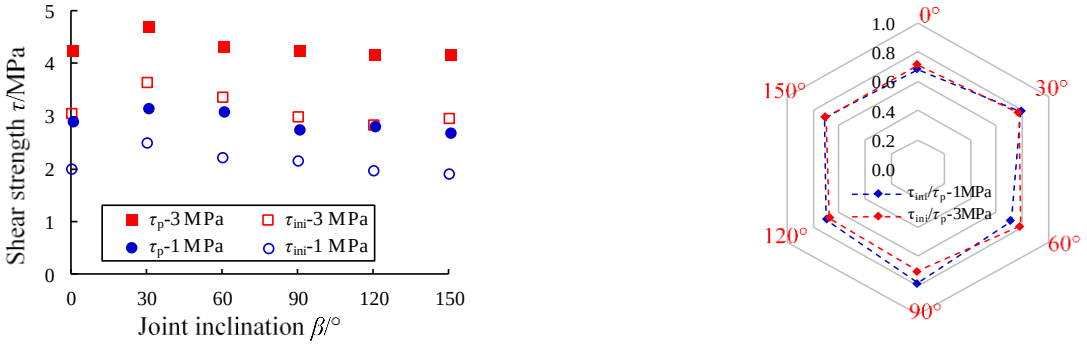

(a) Crack initiation stress (b) Crack initiation level

Fig. 13 The changes of crack initiation stress and initiation level with joint inclination

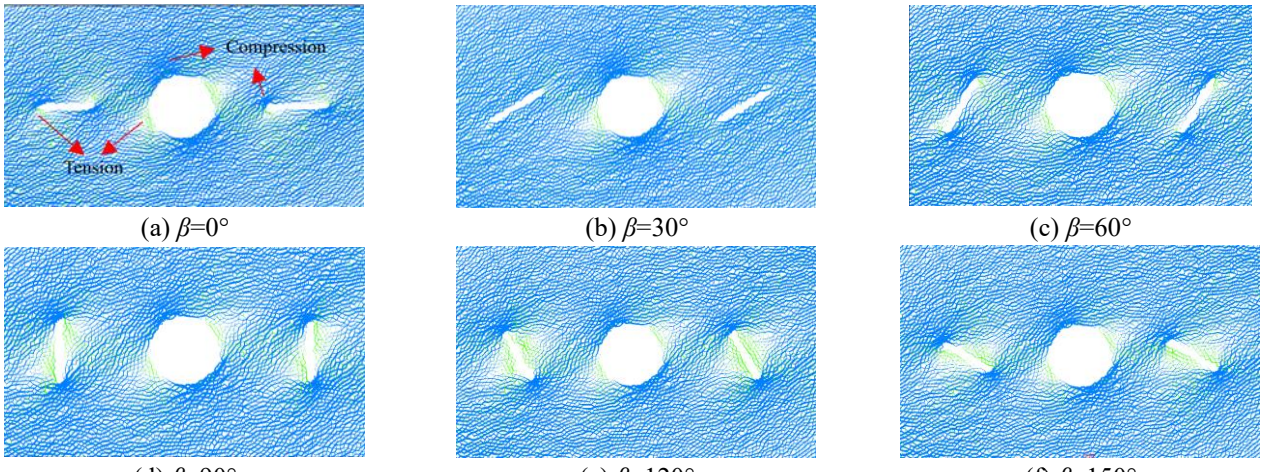

(a) β=0° (b) β=30° (c) β=60°

(d) β=90° (e) β=120° (f) β=150°

Fig. 14 Parallel-bond force distribution around joints and opening at crack initiation

the macro-shear failure of flawed specimen was mainly dominated by the meso-tensile cracks. Comparing the Fig. 11(a) and Fig. 11(b), we can find that the increase of shear cracks starts after the peak stress (i.e., stage III) under the normal stress of 1.0 MPa, while it occurs before the peak stress (i.e., stage II) under the normal stress of 3.0 MPa, almost together with the tensile cracks. This indicates that the increasing normal stress promotes the earlier generation of shear cracks.

Fig. 12 shows the ratio of the number of shear cracks to tensile cracks, i.e., N_s/N_t. From Fig. 12(a), we can see that, at the peak stress, the N_s/N_t at β=30° was obviously larger than other cases, whether under the normal stress of 1.0 or 3.0 MPa. Since the shear strength of rock materials is greater than tensile strength, a larger N_s/N_t, meaning more mobilization of shear resistance capacity of materials, will contribute to a greater shear strength. This explains why the maximum shear strength occurs at β=30°. However, at the stable stage, the N_s/N_t changes not much with the joint inclination, as shown in Fig. 12(b). N_s/N_t is maintained at 0.1~0.15 under the normal stress of 1.0 MPa and 0.22~0.41 under the normal stress of 3.0 MPa.

(a) MCs around joint (b) MCs around opening

Fig. 15 Arrangement of measurement circles (MCs) around flaws

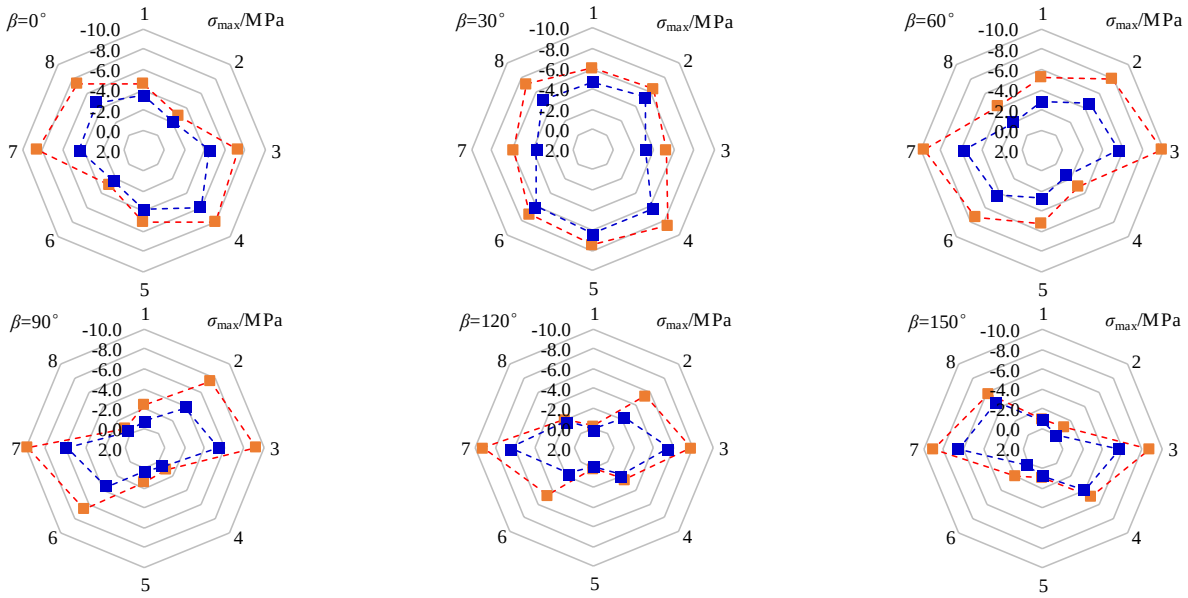

(a) Distribution of σ_{max} around joint

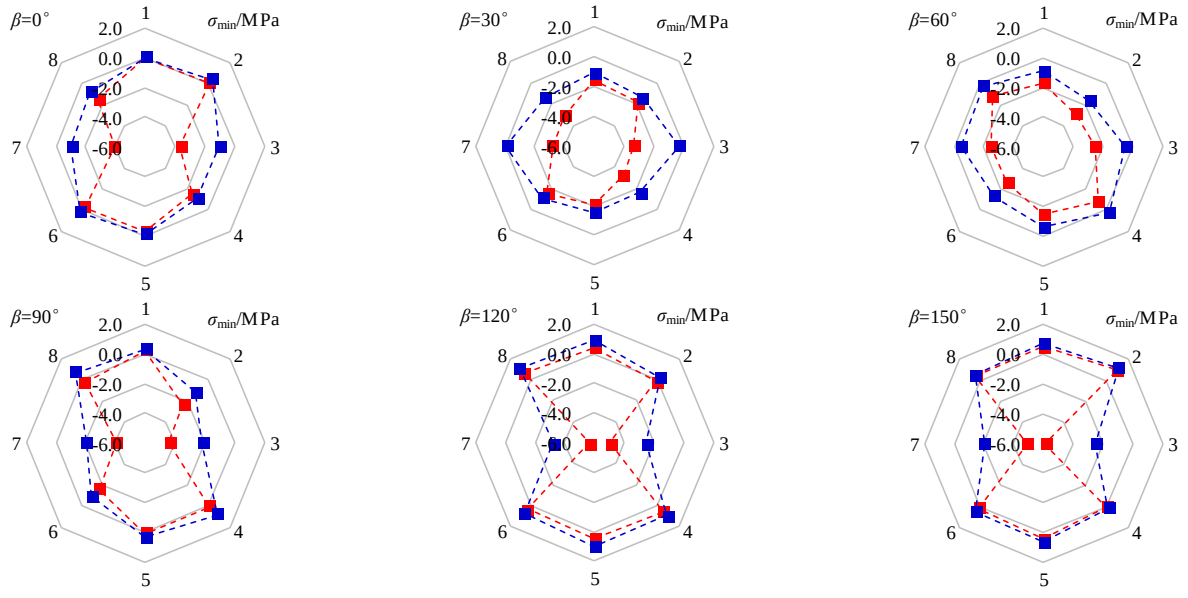

(b) Distribution of σ_{min} around joint

Fig. 16 The distribution of principal stress around the joint

Based on the number of micro-cracks, the crack initiation stress, i.e., τ_{ini}, can also be determined, as shown in Fig. 11. In this research, when the number of micro-cracks reaches 1% of the total number at the peak stress, the shear stress is considered as τ_{ini}. Fig. 13(a) shows that the changes of τ_{ini} with joint inclination is similar to that of τ_p.

Although τ_{ini} and τ_p vary greatly with the joint inclination and normal stress, the cracks initiation level, determined as τ_{ini}/τ_p, changes not much, close to 0.7, as shown in Fig. 13(b).

4.2 Stress fields

The existence of opening and joints has greatly changed

(a) Distribution of σ_{max} around opening

(b) Distribution of σ_{min} around opening

Fig. 17 The distribution of principal stress around the opening

the internal stress state of specimen. Fig. 14 shows the parallel-bond (PB) force distribution around joints and opening just before cracks initiation. The blue areas represent compression and the green areas represent tension.

It can be seen that the stress distribution around joint is greatly affected by the joint inclination. For example, as the β increases from 60° to 180° (i.e., 0°), the tension areas near joint tips (see Fig. 14(c)) gradually move to the middle part of joint (see Figs. 14(d) and 14(e)), and finally reach the other end of joint (see Figs. 14(a)-14(f)). Therefore, Fig. 14(e) can well explain why the micro-cracks initiated from the middle part of joint, rather than tips, at β=120°. However, the compression areas are always near the joint tips, change not much with the joint inclination. However, β=30° shows some differences that no obvious tensile or compressive stress concentration appears around the joints, indicating a more uniform stress state, as shown in Fig. 14(b).

In addition, joint inclination has little effect on the stress distribution around the opening. The compression areas are always located at the top left and bottom right of opening, while tension areas are located at upper-right and lower-left sides of opening, approximately orthogonal to the positions of compression areas, as shown in Fig. 14.

4.3 Principal stress distribution around joints

To quantitatively analyse the stress distribution around the opening and joints, eight measurement circles (MC-1~8) were arranged around the joints and opening, as shown in Fig. 15. Based on the stress components measured by the MCs, the maximum and minimum principal stresses (i.e., σ_{max} and σ_{min}) can be obtained. Note that the negative values indicate compression and positive values indicate tension.

Fig. 16 shows the distribution of principal stress (σ_{max} and σ_{min}) around the joints with different inclinations. From Fig. 16(a), we can see that the higher normal stress increases the σ_{max}s around the joints, indicating enhanced compression areas. Whereas, normal stress has little effect on the distribution shape of σ_{max}. The distribution shape changes dramatically with the joint inclination. Generally, the maximum σ_{max} occurred at MC-3, 7 (i.e., joint tips). For example, when β=60°, the σ_{max}s at MC-3, 7 reaches 10 MPa (σ_n=3.0 MPa) and 6 MPa (σ_n=1.0 MPa), much higher than the initiation stress and peak stress, indicating an intense compressive stress concentration at the joint tips. Also, larger σ_{max}s can also be observed at MC-2, 6 at β=60°~120°, MC-4, 8 at β=0°&150°. Compared with other cases, the distribution of σ_{max}s at β=30° was more uniform and no obvious compressive stress concentrations occurred around joint, which is consistent with that shown in Fig. 14(b). In addition, the minimum σ_{max} usually occurs at MC-2, 6 at β=0°&150°, MC-4, 8 at β=60°&90° and MC-1, 5 at β=120°. The magnitude difference between the maximum and minimum σ_{max} tends to be larger at β=90°~150°, indicating a more uneven distribution of principal stress around joints with a larger inclination.

Fig. 16(b) clearly shows that normal stress has affected the distribution of σ_{min}s around the joint, especially near the joint tips. For example, at β=30°, the σ_{min}s at MC-3 and MC-7 decreased from 0 MPa (σ_n=1.0 MPa) to -3 MPa (σ_n=3.0 MPa), meaning that the tension at joint tips was greatly suppressed by a higher normal stress. The positions of positive σ_{min}s, indicating tension, rotate as the joint inclination changes. Under the normal stress of 1.0 MPa,

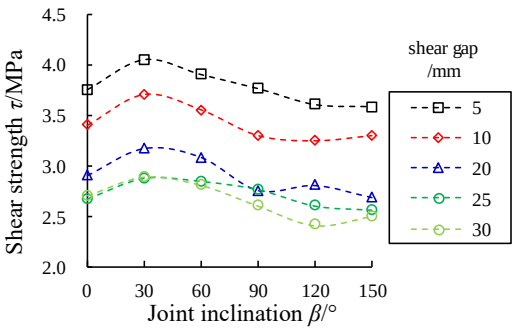

Fig. 18 Effect of gap size on the shear strength of flawed specimens

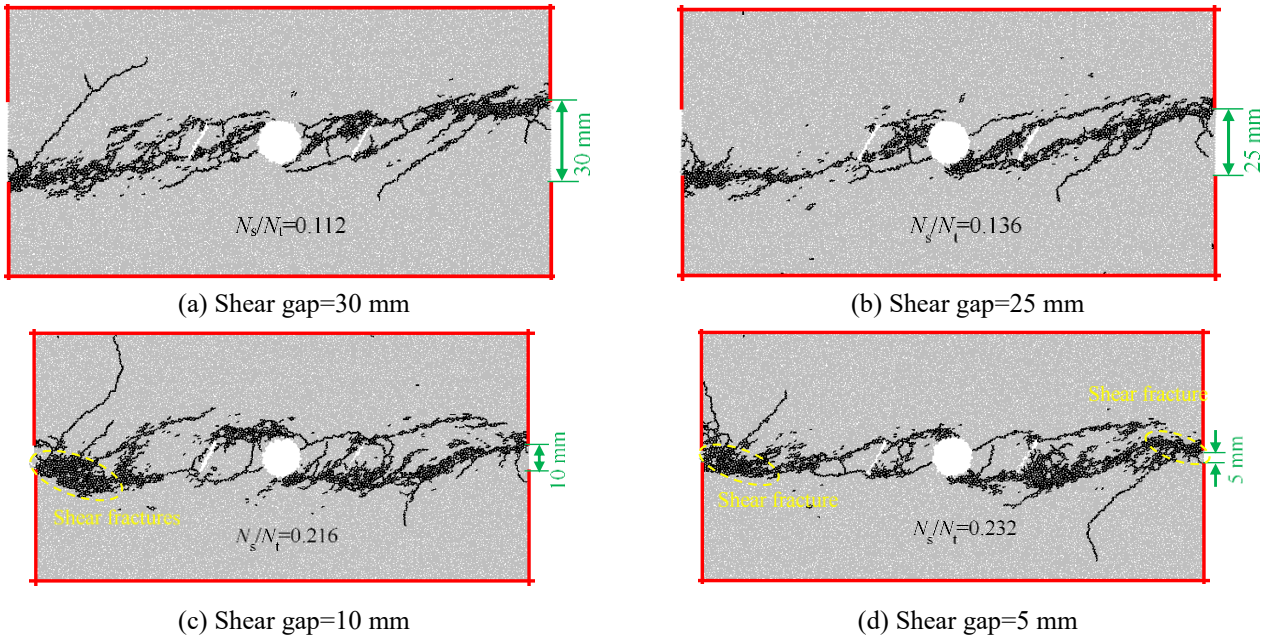

(a) Shear gap=30 mm

(b) Shear gap=25 mm

(c) Shear gap=10 mm

(d) Shear gap=5 mm

Fig. 19 Effect of gap size on the failure patterns of flawed specimens

the positive σ_{min}s, located at MC-4, 8 at β=60°&90°, moved to MC-1, 5 at β=120°, finally to MC-2, 6 at β=150°&0°, which was consistent with the movement of tension areas showed in Fig. 14. However, at β=30°, all σ_{min}s around the joint are negative, indicating that no tension areas exist. The positive σ_{min}s tend to be larger at β=90°~150°, indicating a greater tensile stress concentration, which results in a lower τ_{ini} and τ_p.

4.4 Principal stress distribution around opening

Fig. 17 further shows the distribution of principal stress around the circular opening. It can be seen that the distribution shape of principal stress changes not much with the joint inclination and normal stress. In general, the larger σ_{max}s can be measured at MC-1,8 and MC-4,5 (see Fig. 17(a)), corresponding to the compression areas around the opening (Fig. 14). The positive σ_{min}s mainly occur at MC-2, 6 (see Fig. 17(b)), corresponding to the tension areas of opening.

The joint inclination has a significant effect on the magnitude of principal stress around the opening. In Fig. 17(a), under the same normal stress, the σ_{max}s at MC-8,1 and MC-4,5 are greatly improved when β=30°, indicating greater compressive stress concentration. Meanwhile, the σ_{min}s at MC-2, 6 are also greater at β=30°, meaning that the tensile stress concentration around opening is also stronger, see Fig. 17(b). The above indicates that the existence of 30°-joints tends to simultaneously enhance the compressive and tensile stress concentration around the opening, resulting in a larger principal stress deviation, thus worsening the stress state around opening. Interestingly, at β=30°, the joint itself has a better stress state (Section 4.3). This explains why the failure firstly occurs at the opening, rather than joints, at β=30°. In addition, it can also be found that the increasing normal stress has enhanced the compression, whereas suppressed the tension around opening, which is similar to the effect on joints.

5. Discussion

5.1 Effect of shear gap

For regular direct shear tests of joint surface, the ISRM and ASTM suggest that the gap zone between upper and

lower shear boxes should be at least 10 mm and 5 mm, respectively (ASTM 2008, Muralha *et al.* 2014), to ensure that no contact occurs between the shear boxes and joint surface during the shear process. However, whether this standard is applicable for the flawed specimens in this research should be further discussed, because the flaw size (15 mm) is much larger than the suggested gap size (5 mm or 10 mm).

Fig. 18 shows the effect of gap size on the shear strength of flawed specimens based on numerical simulation. We can see that the shear gap of 5 mm or 10 mm will cause a higher shear strength. Especially when gap is 5 mm, the shear strength is nearly increased by 30%, compared with that of 20 mm. However, when the gap is larger than 20 mm, the shear strength changes not much. Fig. 19 further shows the effect of shear gap on the failure pattern, taking β=60° as an example. We can see that the shear gap significantly affects the failures near the boundaries. When the shear gap is larger than flaw size, such as 25 mm and 30 mm, the direct tensile coalescences usually occur between internal flaws and specimen boundaries, as shown in Figs. 19(a) and 19(b). However, when the gap size is smaller than flaw size, obvious shear fracture bands can be observed near the edges of shear boxes, as shown in Figs. 19(c) and 19(d), which can also be reflected by the increasing proportion of shear cracks (N_s/N_t).

The above indicates that a shear gap, smaller than the flaw size, may cause a greater boundary effects and overestimate the shear strength of flawed specimens. Therefore, for the direct shear tests of flawed specimens, a reasonable shear gap should be chosen according to the flaw size. The gap size, slightly larger than the flaw size, is recommended based on this research.

5.2 Comparison between shear and compression

Most previous studies on the mechanical behavior of flawed rock specimens were based on compression tests, mostly uniaxial compression tests. This research continued to explore it, based on direct shear tests, and observed some different experimental phenomena. To better understand the failure and mechanical behavior of flaws, it is necessary to make some comparisons between shear and compression.

(1) Joint inclination has a significant effect on both shear strength and compressive strength. In general, the maximum compressive strength usually occurs at β=90° (Fan *et al.* 2018, Yang *et al.* 2019), i.e., parallel to the loading direction. However, the maximum shear strength proves to be at β=30° in this study, an acute angle to the shear direction. This difference is essentially determined by the different internal stress distribution, which is caused by different boundary conditions. In fact, whether for compression or shear, the higher strength must be attributed to a more uniform stress state around the flaws, such as the 30°-joint under shear and 90°-joint under compression (Fan *et al.* 2018).

(2) The coalescence failure between joints and opening is more complicated under shear than compression. Compared with the results of Fan *et al.* (2018), we can find that the compressive failures of opening and joints tend to be less connected, only local coalescence failure can be observed between joint and opening. However, under direct shear, the interaction between joint and opening tends to be more intense, which can be reflected by the multiple coalescences through wing cracks, tensile cracks and boundary cracks. The difference of failure patterns between shear and compression is caused by the different stress distribution around flaws. For example, under the shear, the tension areas and compression areas around opening are almost reversed, compared to that under compression.

(3) The cracks type, cracks initiation level and cracks evolution rule under shear are similar to those under compression. Wing cracks originating at the joint tips and tensile cracks originating at the opening can be observed under both shear and compression. These cracks always expand towards the loading boundaries, usually the maximum principal stress direction. In this research, the cracks initiation level under shear was determined near 0.7, which is consistent with 0.6~0.655 under compression (Fan *et al.* 2018). Also, the evolution of the number of micro-cracks during the shear and compression were similar, both undergoing four distinct stages. And, the number of tensile cracks is much larger than that of shear cracks, meaning that both the macroscopic shear and compressive failures are essentially dominated by the mesoscopic tensile damage.

6. Conclusions

• The shear strength (τ_p) of flawed specimens is significantly affected by the joint inclination. The maximum shear strength occurs at β=30°, while the minimum occurs at β=0° or 150°. Under a normal stress of 1.0 MPa, the maximum peak dilation (δ_v^p) and the maximum terminal dilation (δ_v^t) occur at β=120° and β=60°, respectively. Both the minimum δ_v^p and the minimum δ_v^t occur at β=30°. Under a normal stress of 3.0 MPa, the effect of joint inclination on shear strength will be more obvious, whereas the effect on dilation will be greatly reduced.

• The failure patterns of flawed specimens under direct shear are complicated and closely related to the joint inclination. The macro-shear failure of flawed specimen is composed of wing cracks originating from joint tips, tensile cracks originating from opening and boundary cracks. Three basic failure patterns can be classified: Type-I (β=30°), Type-II (β=60° & 90°) and Type-III (β=0°&150°), as shown in Fig. 9.

• During the shear, the active AE events (energy and hits) mainly occur at coalescence failure stage. A higher shear strength usually causes a larger magnitude of peak energy rate, meaning a more intense coalescence failure. At the shear-slip stage, the accumulated hits continuously increase due to the friction of fractures, while accumulated energy increases not much.

• The evolution of the number of micro-cracks usually experiences four stages: quiet stage, initial increase, rapid increase and stable stage. A higher normal stress will promote an earlier generation and larger proportion of shear cracks. A larger number of shear cracks at peak stress, meaning more mobilization of shear resistance capacity of materials, usually contributes to a greater shear strength,

such as at β=30°.

• Around the joint, the compression areas are mainly located near joint tips, while the tension areas moves as the joint inclination changes. At β=30°, no obvious tensile or compressive stress concentrations occur around the joint. However, at a larger joint inclination (β=90°~150°), the stress distribution around joint is more uneven, and tensile stress concentration is also greater.

• Around the opening, the compression areas are usually located at the top-left and bottom-right of opening, while the tension areas are approximately orthogonally located. Joint inclination has little effect on the stress distribution around opening, whereas greatly affects the magnitude. Especially, the existence of 30°-joints will enhance both the compression and tension around the opening, worsening the stress environment of opening.

Acknowledgments

The research described in this paper was financially supported by the China Scholarship Council (201806420027), National Natural Science Foundation of China (51904290) and Natural Science Foundation of Jiangsu Province (BK20180663).

References

Aksoy, C.O., Aksoy, G.G., Guney, A., Ozacar, V. and Yaman, H.E. (2020), "Influence of time-dependency on elastic rock properties under constant load and its effect on tunnel stability", *Geomech. Eng.*, **20**(1), 1-7. https://doi.org/10.12989/gae.2020.20.1.001.

ASTM. (2008), *Standard Test Method for Performing Laboratory Direct Shear Strength Tests of Rock Specimens under Constant Normal Force*, ASTM International, U.S.A.

Bahaaddini, M., Sharrock, G. and Hebblewhite, B.K. (2013), "Numerical investigation of the effect of joint geometrical parameters on the mechanical properties of a non-persistent jointed rock mass under uniaxial compression", *Comput. Geotech.*, **49**, 206-225. https://doi.org/10.1016/j.compgeo.2012.10.012.

Cundall, P.A. and Strack, O.D.L. (1979), "A discrete numerical model for granular assemblies", *Geotechnique*, **29**(1), 47-65. https://doi.org/10.1680/geot.1979.29.1.47.

Fakhimi, A., Carvalho, F., Ishida, T. and Labuz, J.F. (2002), "Simulation of failure around a circular opening in rock", *Int. J. Rock Mech. Min. Sci.*, **39**(4), 507-515. https://doi.org/10.1016/S1365-1609(02)00041-2.

Fan, X., Li, K., Lai, H., Xie, Y., Cao, R. and Zheng, J. (2018), "Internal stress distribution and cracking around flaws and openings of rock block under uniaxial compression: A particle mechanics approach", *Comput. Geotech.*, **102**, 28-38. https://doi.org/10.1016/j.compgeo.2018.06.002.

Gay, N.C. (1976), "Fracture growth around openings in large blocks of rock subjected to uniaxial and biaxial compression", *Int. J. Rock Mech. Min. Sci. Geomech. Abstr.*, **13**(8), 231-243. https://doi.org/10.1016/0148-9062(76)91543-6.

Hao, Y.H. and Azzam, R. (2005), "The plastic zones and displacements around underground openings in rock masses containing a fault", *Tunn. Undergr. Sp. Tech.*, **20**(1), 49-61. https://doi.org/10.1016/j.tust.2004.05.003.

Hoek, E. and Brown, E.T. (1997), "Practical estimates of rock mass strength", *Int. J. Rock Mech. Min. Sci.*, **34**(8), 1165-1186. https://doi.org/10.1016/S1365-1609(97)80069-X.

Jeon, S., Kim, J., Seo, Y. and Hong, C. (2004), "Effect of a fault and weak plane on the stability of a tunnel in rock-a scaled model test and numerical analysis", *Int. J. Rock Mech. Min. Sci.*, **41**, 658-663. https://doi.org/10.1016/j.ijrmms.2004.03.115.

Jiang, Y., Xiao, J., Tanabashi, Y. and Mizokami, T. (2004), "Development of an automated servo-controlled direct shear apparatus applying a constant normal stiffness condition", *Int. J. Rock Mech. Min. Sci.*, **41**(2), 275-286. https://doi.org/10.1016/j.ijrmms.2003.08.004.

Kim, J.S., Kim, G.Y., Baik, M.H., Finsterle, S. and Cho, G.C. (2019), "A new approach for quantitative damage assessment of in-situ rock mass by acoustic emission", *Geomech. Eng.*, **18**(1), 11-20. https://doi.org/10.12989/gae.2019.18.1.011.

Lajtai, E.Z. (1969), "Strength of discontinuous rocks in direct shear", *Geotechnique*, **19**(2), 218-233. https://doi.org/10.1680/geot.1969.19.2.218.

Manouchehrian, A., Sharifzadeh, M., Marji, M.F. and Gholamnejad, J. (2014), "A bonded particle model for analysis of the flaw orientation effect on crack propagation mechanism in brittle materials under compression", *Arch. Civ. Mech. Eng.*, **14**(1), 40-52. https://doi.org/10.1016/j.acme.2013.05.008.

Martin, C.D. (1997), "Seventeenth Canadian geotechnical colloquium: The effect of cohesion loss and stress path on brittle rock strength", *Can. Geotech. J.*, **34**(5), 698-725. https://doi.org/10.1139/t97-030.

Matsuki, K., Nakama, S. and Sato, T. (2009), "Estimation of regional stress by FEM for a heterogeneous rock mass with a large fault", *Int. J. Rock Mech. Min. Sci.*, **46**(1), 31-50. https://doi.org/10.1016/j.ijrmms.2008.03.005.

Muralha, J., Grasselli, G., Tatone, B., Blümel, M., Chryssanthakis, P. and Jiang, Y. (2014), "ISRM suggested method for laboratory determination of the shear strength of rock joints: revised version", *Rock Mech. Rock Eng.*, **47**(1), 291-302. https://doi.org/10.1007/s00603-013-0519-z.

Park, K. (2017), "Simple solutions of an opening in elastic-brittle plastic rock mass by total strain and incremental approaches", *Geomech. Eng.*, **13**(4), 585-600. https://doi.org/10.12989/gae.2017.13.4.585.

Sagong, M., Park, D., Yoo, J. and Lee, J.S. (2011), "Experimental and numerical analyses of an opening in a jointed rock mass under biaxial compression", *Int. J. Rock Mech. Min. Sci.*, **48**(7), 1055-1067. https://doi.org/10.1016/j.ijrmms.2011.09.001.

Yang, S.Q., Yin, P.F., Zhang, Y.C., Chen, M., Zhou, X.P., Jing, H.W. and Zhang, Q.Y. (2019), "Failure behavior and crack evolution mechanism of a non-persistent jointed rock mass containing a circular hole", *Int. J. Rock Mech. Min. Sci.*, **114**, 101-121. https://doi.org/10.1016/j.ijrmms.2018.12.017.

Zhang, Y., Jiang, Y., Asahina, D. and Wang, C. (2020), "Experimental and numerical investigation on shear failure behavior of rock-like samples containing multiple non-persistent joints", *Rock Mech. Rock Eng.*, **53**(10), 4717-4744. https://doi.org/10.1007/s00603-020-02186-0.

Zhuang, X., Chun, J. and Zhu, H. (2014), "A comparative study on unfilled and filled crack propagation for rock-like brittle material", *Theor. Appl. Fract. Mech.*, **72**, 110-120. https://doi.org/10.1016/j.tafmec.2014.04.004.

CC